

This is a repository copy of *Fully-relativistic electron Bernstein wave current drive simulations in the STEP spherical tokamak*.

White Rose Research Online URL for this paper:

<https://eprints.whiterose.ac.uk/219592/>

Version: Accepted Version

Article:

Biswas, Bodhi orcid.org/0000-0001-7993-3732, Freethy, Simon and Vann, Roddy orcid.org/0000-0002-3105-2546 (Accepted: 2024) Fully-relativistic electron Bernstein wave current drive simulations in the STEP spherical tokamak. Nuclear Fusion. ISSN 1741-4326 (In Press)

<https://doi.org/10.1088/1741-4326/ad8fbc>

Reuse

This article is distributed under the terms of the Creative Commons Attribution (CC BY) licence. This licence allows you to distribute, remix, tweak, and build upon the work, even commercially, as long as you credit the authors for the original work. More information and the full terms of the licence here:

<https://creativecommons.org/licenses/>

Takedown

If you consider content in White Rose Research Online to be in breach of UK law, please notify us by emailing eprints@whiterose.ac.uk including the URL of the record and the reason for the withdrawal request.

ACCEPTED MANUSCRIPT • OPEN ACCESS

Fully-relativistic electron Bernstein wave current drive simulations in the STEP spherical tokamak

To cite this article before publication: Bodhi Biswas *et al* 2024 *Nucl. Fusion* in press <https://doi.org/10.1088/1741-4326/ad8fbc>

Manuscript version: Accepted Manuscript

Accepted Manuscript is “the version of the article accepted for publication including all changes made as a result of the peer review process, and which may also include the addition to the article by IOP Publishing of a header, an article ID, a cover sheet and/or an ‘Accepted Manuscript’ watermark, but excluding any other editing, typesetting or other changes made by IOP Publishing and/or its licensors”

This Accepted Manuscript is © 2024 The Author(s). Published by IOP Publishing Ltd on behalf of the IAEA.



As the Version of Record of this article is going to be / has been published on a gold open access basis under a CC BY 4.0 licence, this Accepted Manuscript is available for reuse under a CC BY 4.0 licence immediately.

Everyone is permitted to use all or part of the original content in this article, provided that they adhere to all the terms of the licence <https://creativecommons.org/licenses/by/4.0>

Although reasonable endeavours have been taken to obtain all necessary permissions from third parties to include their copyrighted content within this article, their full citation and copyright line may not be present in this Accepted Manuscript version. Before using any content from this article, please refer to the Version of Record on IOPscience once published for full citation and copyright details, as permissions may be required. All third party content is fully copyright protected and is not published on a gold open access basis under a CC BY licence, unless that is specifically stated in the figure caption in the Version of Record.

View the [article online](#) for updates and enhancements.

Fully-relativistic electron Bernstein wave current drive simulations in the STEP spherical tokamak

Bodhi Biswas^{*1}, Simon Freethy², and Roddy Vann¹

¹York Plasma Institute. School of Physics, Engineering & Technology, University of York. York, UK.

²UKAEA, Culham Campus, Abingdon, UK.

Compiled on October 27, 2024

Abstract

Electron Bernstein waves (EBWs) are theorised to efficiently drive current in spherical tokamak power plants, e.g. Spherical Tokamak for Energy Production (STEP). At high temperatures ($T_e \gtrsim 4$ keV), relativistic effects can significantly impact wave propagation. This work presents relativistic calculations of EBW wave propagation, damping, and current drive (CD) in a conceptual STEP plasma. Kramers-Kronig relations are exploited to efficiently evaluate the fully-relativistic dispersion relation for arbitrary wave-vectors, leading to a $>50x$ speed-up compared to previous efforts. Current drive efficiency is calculated using both linear and quasilinear codes. Thus, for the first time, large parametric scans of fully-relativistic EBW CD simulations are performed through ray-tracing. In STEP, three main classes of rays are identified. The first class propagate deep into the core ($\rho < 0.5$), but exist only if relativistic effects are accounted for. They damp strongly at the fundamental harmonic on nearly-thermal electrons and thus drive little current. A second class of rays propagate to intermediate depths ($\rho \approx 0.3 - 0.7$) before damping at the 2nd harmonic. Their CD efficiencies are significantly altered due to relativistic changes to trajectory and polarisation. The third class of rays damp strongly far off-axis ($\rho > 0.7$), predominantly at the second harmonic. These ray trajectories are sufficiently short and “cold” that relativistic effects are unimportant. In linear CD simulations, the optimal launch point corresponds to this third class of rays, suggesting that non-relativistic simulations are adequate. However, quasilinear calculations indicate that, at reactor relevant powers, current drive is maximised at $\rho \approx 0.6$. This quasilinear optimal point corresponds to the second class of rays, for which relativistic propagation does matter.

1 Introduction

Electron Bernstein waves (EBWs) can drive toroidal current in tokamaks by asymmetrically damping on a resonant electron population. EBWs do not have a density cutoff, making them attractive as a current drive actuator in overdense plasmas ($\omega_{pe} > \Omega_e$, where ω_{pe} and Ω_e are the electron plasma and electron cyclotron frequency, respectively) [1]. For example, off-axis EBW current drive (EBCD) is expected to be three times as efficient as electron cyclotron current drive during steady-state operation in STEP [2–4]. It is therefore being strongly considered as a current-drive actuator for STEP, where >100 MW of microwave power (delivered by hundreds of 1 MW class gyrotrons) will be used to deliver ~ 4 MA of auxiliary steady-state current. The resulting current-drive system requires significant recirculating power. Its efficiency is a critical factor in optimising Q_{eng} .

^{*}Corresponding author: bodhi.biswas@york.ac.uk

1
2
3
4
5
6
7
8
9
10
11
12
13
14
15
16
17
18
19
20
21
22
23
24
25
26
27
28
29
30
31
32
33
34
35
36
37
38
39
40
41
42
43
44
45
46
47
48
49
50
51
52
53
54
55
56
57
58
59
60

EBWCD performance can be sensitive to plasma and launch conditions, and so accurate modelling of wave propagation, damping, and electron response is necessary. Propagation is typically modelled using ray-tracing, while Fokker-Planck codes model damping and the electron response [5,6]. Relativistic effects can significantly impact wave *damping* and the *electron current response*. Relativistic fast electrons shift and broaden the cyclotron resonance, and it is standard practice to model these effects. A relativistic population also impacts current drive (CD) efficiency through the modification of collisionality, and is therefore routinely modelled in linear and quasilinear CD codes. In both cases, the direct, relativistic interaction between the EBW and the electrons is limited to the cyclotron resonance curve in momentum-space.

Relativistic *propagation* may also be important at reactor-relevant temperatures. Modifications to the wave trajectory in (\mathbf{r}, \mathbf{k}) -space and its polarisation will affect CD performance. In addition, relativistic effects cause a narrowing of the low-field-side cyclotron resonance [7]. In simulations that employ relativistic damping but non-relativistic ray trajectories, this narrowing can cause the weak-damping approximation to break (making ray-tracing invalid) prior to the complete depletion of ray power. This problem is frequently encountered in STEP simulations for rays that propagate sufficiently far into the core ($\rho < 0.4$) and approach the fundamental harmonic. To model this parameter regime, and to ensure accuracy elsewhere, requires simulating relativistic propagation.

This is challenging. Unlike the resonant damping, propagation requires evaluating the Hermitian contribution to the dielectric tensor. Doing so for the fully-relativistic, kinetic dispersion is numerically cumbersome. Trubnikov first derived the fully-relativistic dispersion by linearising the Vlasov equation and applying the method of unperturbed orbits [8]. Treating the time integral analytically produces a 2D velocity integral $(v_{\perp}, v_{\parallel})$ that must be evaluated numerically. This is Trubnikov's "1st Form". The integrand quickly decays with $|v|$, but numerical challenges persist due to poles along resonance curves. Weiss developed a numeric technique for this integral [9], but it is still slow because it is 2D. Trubnikov's "2nd Form" treats the velocity integral analytically, leaving a 1D time integral that must be evaluated numerically. This is typically faster to evaluate than the 1st Form. However, the integrand is highly oscillatory in time and roughly decays as $\exp(-|N_{\parallel}|t)$, where N_{\parallel} is the parallel refractive index. In a toroidal geometry, N_{\parallel} is not conserved and can become arbitrarily small, leading to significant slowing down of the ray-tracer. Previous efforts to simulate relativistic EBW propagation and damping use approximate slab-geometries such that the ray-tracing equations are not needed [7, 10]. One notable exception is ray-tracing studies in ARIES-ST by Nelson-Melby *et al.* [11]. They report that each ray simulation requires several wall-clock hours (as opposed to several seconds for a non-relativistic ray). Such numerical expense has made difficult a thorough investigation of the effects of relativistic propagation on current drive.

Numerous efforts have been made at approximating the fully-relativistic dispersion [12–16]. These are commonly referred to as “weakly-” or “moderately-”relativistic treatments since they take the limit $\mu_e \equiv c^2/v_{te}^2 \gg 1$, where c is the speed of light and $v_{te} = \sqrt{T_e/m_e}$ is the thermal electron velocity. These formulations are often also constrained to small N_{\parallel} and either the small or large λ limit (where $\lambda = \mu_e^{-1}(N_{\perp}/Y)^2$ is the Larmor-radius parameter and $Y \equiv \Omega_e/\omega$). A helpful review of various weakly relativistic dispersions can be found in Volpe *et al.* and references therein [16]. Constraints on Larmor radius are particularly limiting for EBWs, as λ can span from $\ll 1$ prior to X-B mode-conversion, to $\gtrsim 1$ afterwards. Constraints on λ aside, the validity of weakly-relativistic models is questionable for reactor-relevant temperatures ($T_e \sim 20$ keV or equivalently $\mu_e^{-1} \sim 0.04$).

This work applies a fully-relativistic kinetic dispersion to the problem of O-X-B launch,

both in a slab and toroidal geometry. (Here, “O”, “X”, and “B” denote the cold ordinary and extra-ordinary modes, and the EBW, respectively.) Following Pavlov and Castejon [17], the Kramers-Kronig relations are exploited to efficiently evaluate the Hermitian part of the fully-relativistic dielectric tensor. (It is relatively easy to evaluate the anti-Hermitian part of the fully-relativistic dielectric tensor.) At low N_{\parallel} , the result is a numeric scheme that is $\sim 100x$ faster than direct evaluation of Trubnikov’s 2nd form. Its accuracy is exact, and its efficiency is independent of N_{\parallel} . (Consequently, it is also applicable to the study of direct X-B launch at low N_{\parallel} .)

A ray-tracer is developed to solve fully-relativistic EBW trajectories in a toroidal geometry. It is coupled to a linear adjoint model [18] to provide quick estimates of current drive at low microwave power. The ray-tracer is also coupled to CQL3D [19] to account for quasilinear effects at high powers. In doing so, the impact of relativistic propagation on CD efficiency is modelled for the first time. This modelling workflow is applied to a conceptual STEP plasma to demonstrate important relativistic effects that are presently neglected in non-relativistic simulations. We highlight a particular class of relativistic rays that propagate deep into the STEP plasma ($\rho < 0.5$) and strongly damp at the fundamental harmonic. These rays cannot be modelled with a non-relativistic dispersion without the weak-damping approximation breaking.

Section 2 formulates the numeric scheme for evaluating the fully-relativistic dispersion using Kramers-Kronig relations. Section 3 tests this dispersion against others by evolving the ray-tracing equations in a slab geometry. Section 4 applies this model to a toroidal ray-tracer with STEP plasma parameters. The impact of relativistic effects on CD efficiency is discussed, both in the linear (low-power) and quasilinear (high-power) regime. Section 5 summarises these findings, and conclude that relativistic propagation is indeed important to model in STEP.

2 Fast evaluation of relativistic dispersion

We seek to construct a fast, numerically robust method to evaluate the fully-relativistic EBW dispersion relation. We start with Trubnikov’s 1st Form [8, 20]. It is assumed that the wave frequency is much larger than the ion cyclotron and ion plasma frequencies ($\omega \gg \Omega_i, \omega_{pi}$) and so ion dynamics can be ignored. The susceptibility tensor in Stix coordinates [21] is

$$\chi_{ij} = \sum_{n=-\infty}^{\infty} \chi_{ij}^n \quad (1a)$$

$$\chi_{ij}^n = -\frac{X}{2} \frac{\mu_e^2}{K_2(\mu_e)} F_{ij}^n \quad (1b)$$

$$F_{ij}^n = \int_{-\infty}^{\infty} d\bar{p}_{\parallel} \int_0^{\infty} d\bar{p}_{\perp} \bar{p}_{\perp} \frac{e^{-\mu_e \gamma_e}}{\gamma_e} \frac{P_{ij}^n}{\gamma_e - N_{\parallel} \bar{p}_{\parallel} - nY} \quad (1c)$$

where $X \equiv \omega_{pe}^2/\omega^2$, K_2 is the MacDonalld function of 2nd type, $\bar{p} \equiv p/(m_e c)$ is normalised particle momentum, $\gamma_e = \sqrt{1 + \bar{p}^2}$ is the Lorentz factor, and n is the cyclotron harmonic. The subscripts “ \parallel ” and “ \perp ” denote the parallel and perpendicular component with respect to the background magnetic field. The dyadic elements P_{ij}^n are functions of \bar{p}_{\parallel} , \bar{p}_{\perp} , ν_{\parallel} , and ν_{\perp} , where $\nu \equiv N/Y$. These elements are

$$P_{11}^n = \frac{n^2}{\nu_{\perp}^2} J_n^2 \quad (2a)$$

$$P_{12}^n = -P_{21}^n = \frac{i\bar{p}_\perp n}{\nu_\perp} J_n J_n' \quad (2b)$$

$$P_{13}^n = P_{31}^n = -\frac{\bar{p}_\parallel n}{\nu_\perp} J_n^2 \quad (2c)$$

$$P_{22}^n = \bar{p}_\perp^2 J_n^2 \quad (2d)$$

$$P_{23}^n = -P_{32}^n = i\bar{p}_\parallel \bar{p}_\perp J_n J_n' \quad (2e)$$

$$P_{33}^n = \bar{p}_\parallel^2 J_n^2 \quad (2f)$$

where $J_n = J_n(\nu_\perp \bar{p}_\perp)$ is the Bessel function of the 1st kind, and J_n' is its first derivative.

The variable change $\bar{p}_\perp \rightarrow \gamma_e$ is taken, resulting in

$$F_{ij}^n = \int_{-\infty}^{\infty} d\bar{p}_\parallel I_{ij}^n(\bar{p}_\parallel) \quad (3a)$$

$$I_{ij}^n(\bar{p}_\parallel) = \int_1^{\infty} d\gamma_e e^{-\mu_e \gamma_e} \frac{P_{ij}^n}{\gamma_e - N_\parallel \bar{p}_\parallel - nY} \quad (3b)$$

The integrand in eq. 3b has a pole at

$$\gamma_e = N_\parallel \bar{p}_\parallel + nY \equiv \gamma_e^n \quad (4)$$

This pole represents the wave-particle resonance, and therefore contributes to the anti-Hermitian (AH) component of the susceptibility χ . We rewrite:

$$I_{ij}^n(\bar{p}_\parallel) = I_{ij}^{n,H} + iI_{ij}^{n,AH} \quad (5a)$$

$$I_{ij}^{n,H} = \mathcal{P} \int_1^{\infty} d\gamma_e e^{-\mu_e \gamma_e} \frac{P_{ij}^n}{\gamma_e - \gamma_e^n} \quad (5b)$$

$$I_{ij}^{n,AH} = \pm \pi e^{-\mu_e \gamma_e^n} P_{ij}^n(\bar{p}_\perp(\bar{p}_\parallel, \gamma_e^n)) \quad (5c)$$

where H denotes the Hermitian part, and \mathcal{P} denotes the principal value. In eq. 5c, \bar{p}_\perp is evaluated at the pole and is therefore a function of \bar{p}_\parallel and γ_e^n , in accordance with eq. 4. The Sokhotski-Plemelj theorem has been used. The ambiguity regarding the \pm -sign in eq. 5c is resolved by following the Landau prescription. Expanding around the pole in ω_i reveals $\gamma_e^n \approx (ck_\parallel \bar{p}_\parallel + n\Omega_e)(\omega_r - i\omega_i)/\omega_r^2$. Next, for a wave with positive real frequency, $ck_\parallel \bar{p}_\parallel + n\Omega_e > 0$ must hold for the wave-particle resonance to exist. With these two considerations, it follows that the pole must be kept *below* the integration contour in complex γ_e -space. Accordingly, the minus-sign should be used.

The AH component of F_{ij}^n is simply

$$F_{ij}^{n,AH} = -\pi \int_{-\infty}^{\infty} d\bar{p}_\parallel e^{-\mu_e \gamma_e^n} P_{ij}^n(\bar{p}_\perp(\bar{p}_\parallel, \gamma_e^n)) \quad (6)$$

Equation 6 is a 1D integral along the resonance curve in momentum-space. The integration domain is bounded for $|N_\parallel| < 1$. Even for $|N_\parallel| \geq 1$, the integrand quickly decays as γ_e^n grows. Substitution into eq. 1b then provides

$$\chi_{ij}^{n,AH} = -\frac{X}{2} \frac{\mu_e^2}{K_2(\mu_e)} F_{ij}^{n,AH} \quad (7)$$

Kramers-Kronig (KK) relations [22, 23] can be exploited to quickly evaluate $\chi_{ij}^{n,H}$. Their application to linear plasma waves is reported in Brambilla's textbook [24]. Pavlov and Castejon [17] have recently applied such a strategy to evaluating the fully-relativistic

EBW dispersion relation. This paper applies a slightly different formulation which is quantitatively identical.

Suppose one wishes to evaluate $\mathcal{F}(\omega, \mathbf{k}) = \mathcal{G}(\omega, \mathbf{k}) + i\mathcal{Q}(\omega, \mathbf{k})$, where \mathcal{G} and \mathcal{Q} are real. Assume \mathcal{F} is analytic in the upper-half plane in complex ω -space and decays such that $\lim_{\omega \rightarrow \pm\infty} |\mathcal{F}| \rightarrow 0$. Then the following KK relations apply:

$$\mathcal{G}(\omega, \mathbf{k}) = \frac{1}{\pi} \mathcal{P} \int_{-\infty}^{+\infty} \frac{\mathcal{Q}(\omega', \mathbf{k})}{\omega' - \omega} d\omega' \quad (8a)$$

$$\mathcal{Q}(\omega, \mathbf{k}) = -\frac{1}{\pi} \mathcal{P} \int_{-\infty}^{+\infty} \frac{\mathcal{G}(\omega', \mathbf{k})}{\omega' - \omega} d\omega' \quad (8b)$$

We limit the integration to positive ω by taking eqs. 8 and multiplying the numerator and denominator by $(\omega' + \omega)$. This results in

$$\mathcal{G}(\omega, \mathbf{k}) = \begin{cases} \frac{2}{\pi} \mathcal{P} \int_0^{+\infty} \frac{\omega' \mathcal{Q}(\omega', \mathbf{k})}{\omega'^2 - \omega^2} d\omega' & \text{if } \mathcal{Q}(\omega) \text{ is even.} \\ \frac{2\omega}{\pi} \mathcal{P} \int_0^{+\infty} \frac{\mathcal{Q}(\omega', \mathbf{k})}{\omega'^2 - \omega^2} d\omega' & \text{if } \mathcal{Q}(\omega) \text{ is odd.} \end{cases} \quad (9)$$

and a similar relation for $\mathcal{Q}(\omega, \mathbf{k})$. Thus, eqs. 9 can be used to evaluate

$$\chi_{ij}^{n,H}(\omega, \mathbf{k}) = \begin{cases} \frac{2}{\pi} \mathcal{P} \int_0^{+\infty} \frac{\omega' \chi_{ij}^{n,AH}(\omega', \mathbf{k})}{\omega'^2 - \omega^2} d\omega' & (i, j) = (1,1), (1,3), (2,2), (3,3) \\ \frac{2\omega}{\pi} \mathcal{P} \int_0^{+\infty} \frac{\chi_{ij}^{n,AH}(\omega', \mathbf{k})}{\omega'^2 - \omega^2} d\omega' & (i, j) = (1,2), (2,3) \end{cases} \quad (10)$$

Note that $\chi_{ij}^{n,H}$ and $\chi_{ij}^{n,AH}$ are not restricted to purely real functions. This can be shown by separating $\chi_{ij}^{n,H}$, $\chi_{ij}^{n,AH}$ into real and imaginary parts and applying the KK relations to each. Evaluating $\chi_{ij}^{n,H}$ requires a single 1D integration along ω' in the ‘‘outer loop’’, and 1D integrations along γ_e in the ‘‘inner loop’’ to evaluate $\chi_{ij}^{n,AH}(\omega')$ (see eq. (6-7)). The integration domain of the outer loop can be further bounded by realising that the resonance curve exists only for $n^2 Y^2 + N_{\parallel}^2 > 1$. Accordingly, the upper-bound of the integration in eq. 10 is truncated to $\omega' < \Omega_e \sqrt{n^2 + N_{\parallel}^2 / Y^2}$. In this domain, the integrand is smooth, allowing for an efficient Gaussian-quadrature scheme. The singularity at $\omega' = \omega$ is handled using techniques similar to those described in Section 3 of Weiss [9].

Through the KK relations, $\chi_{ij}^{n,H}$ is roughly proportional to $\chi_{ij}^{n,AH}$. Therefore, only the the cyclotron harmonic minimising $|1 - nY|$ - and its neighbouring harmonics - will be non-negligible. Correspondingly, only a few terms in the series are needed for convergence. More terms are needed in the presence of strong harmonic overlap (i.e. if T_e and $|N_{\parallel}|$ are sufficiently large).

Figure 1 plots the speed at which the fully-relativistic dispersion is evaluated using the KK method. It is compared against an optimised evaluation of Trubnikov’s 2nd formula using numeric techniques borrowed from the code R2D2 [7]. (A direct evaluation of Trubnikov’s 1st formula, without the use of KK relations, is not plotted. It is much too slow.) Trubnikov’s 2nd form is faster at high N_{\parallel} . However, as N_{\parallel} drops, the dispersion relation becomes increasingly slow to converge. This can be particularly problematic in toroidal geometries, where N_{\parallel} along a ray is not conserved and can become small. In some cases, a single ray trajectory can take several hours as it approaches very small N_{\parallel} . In contrast, the speed of convergence for the KK-formula is independent of N_{\parallel} , making it clearly favorable in situations where $N_{\parallel} \lesssim 0.65$. (This N_{\parallel} , at which both methods

perform equally well, is weakly sensitive to other wave parameters.) In toroidal geometry (see Section 4), an optimised ray-tracing scheme will be employed to switch between the two dispersions depending on N_{\parallel} .

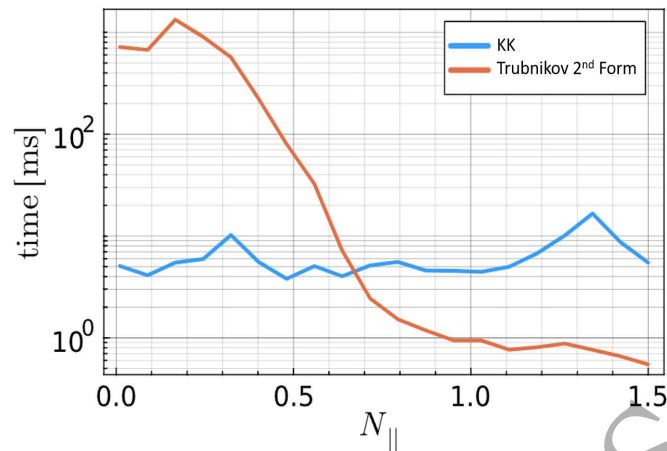


Figure 1: Benchmark of speed at which the fully-relativistic dispersion relation is numerically evaluated. A relative error tolerance of 10^{-7} is used. Speed of evaluating Trubnikov's 2nd Form is strongly dependent on N_{\parallel} . Wave-parameters: $N_{\perp} = 5$, $X = 1.3$, $Y = 0.66$, $\mu_e^{-1} = 0.02$. Test conducted with the *Julia* bench-marking tool *BenchmarkTools.jl* and using a AMD Ryzen 7 3700X 4.05GHz CPU.

3 Relativistic effects in slab geometry

Calculation of the fully relativistic dispersion using the KK relations is verified in a ray-tracing simulation of O-X-B launch in slab geometry. Details of the ray-tracer can be found in Appendix A. The magnetic field is directed along the z -direction, while density varies in the x -direction. A hyperbolic tangent function is used for the density profile, as shown in Figure 2. The density gradient at the cutoff is set to $k_0 L_n = 10$, with k_0 being the vacuum wave-number and $L_n \equiv n_e/|\partial_x n_e|$ being the density scale-length.

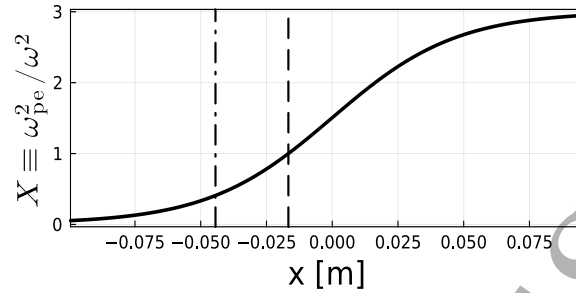


Figure 2: Density profile in slab geometry. Dashed vertical line denotes O-mode density cutoff ($X = 1$). Dash-dotted vertical line denotes the upper hybrid resonance (UHR), which corresponds to $X + Y^2 = 1$.

An O-mode is launched into the high-density region at the optimal angle for O-X mode-conversion ($N_{\parallel} \equiv N_z = \sqrt{Y/(1+Y)}$). In these runs, the magnetic field is uniform and $Y = 0.77$ everywhere. Electron temperature is 1keV. Figure 3 shows the ray trajectory in real-space (left) and phase-space (right) as a function of x . Three dispersion relations are plotted: (1) the non-relativistic, warm dispersion, (2) the fully-relativistic KK formula, and (3) the fully-relativistic Trubnikov 2nd form. The latter two should be quantitatively identical, which enables the benchmarking of our code. The three dispersions show excellent agreement until the X-mode begins converting to the EBW, at which point the non-relativistic dispersion slightly over-estimates N_{\perp} . In addition, the non-relativistic ray travels slightly more obliquely (in the z direction). These results indicate a slight disagreement between the non-relativistic and relativistic Bernstein modes.

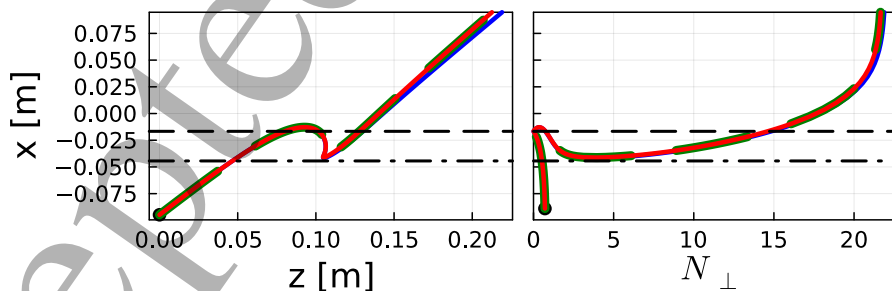


Figure 3: Ray trajectories in slab geometry (see Fig. 2) with $T_e = 1\text{keV}$. Blue: non-relativistic. Red: KK. Green dashed: Trubnikov 2nd Form. Dashed line denotes the O-Mode cutoff. Dash-dotted line denotes the UHR.

Figure 4 repeats the previous exercise at $T_e = 4\text{keV}$. The disagreement in ray trajectories following the X-B mode-conversion is now significantly larger. Note that STEP operates with a pedestal temperature of $\sim 4\text{keV}$, which coincides with the UHR. This suggests that relativistic propagation may significantly impact EBCD.

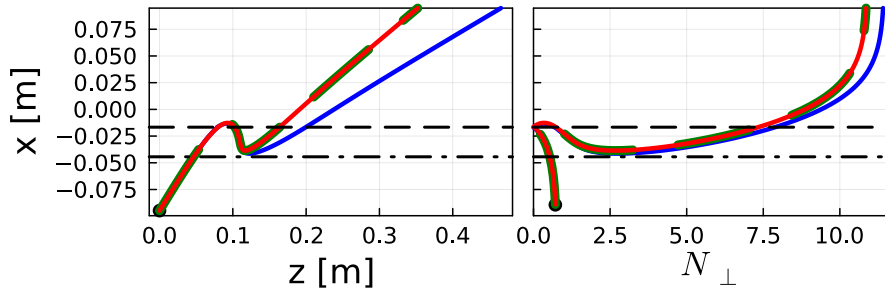


Figure 4: Ray trajectories in slab geometry (see Fig. 2) with $T_e = 4\text{keV}$. Blue: non-relativistic. Red: KK. Green dashed: Trubnikov 2nd Form. Dashed line denotes the O-Mode cutoff. Dash-dotted line denotes the UHR.

This exercise is repeated for $T_e = 15\text{keV}$, which is more representative of core temperatures in a fusion power plant. Since ray-tracing is being employed, we must check that the weak-damping condition remains valid along the trajectory ($|\text{Im}(N_\perp)| \ll \text{Re}(N_\perp)$). This requires keeping $T_e \approx 3\text{keV}$ near the UHR, and then ramping up T_e sufficiently far away from this region. One such temperature profile is shown in Figure 5. The resulting dispersion relation and ray trajectories are shown in Figure 6. The non-relativistic ray strongly diverges in both real and phase-space at $T_e \gtrsim 10\text{keV}$. The reason for this disagreement can be gleaned from plotting $|\text{Im}(N_\perp)|/\text{Re}(N_\perp)$ along the rays. As T_e increases, the non-relativistic ray strongly damps at the Doppler-broadened 1st harmonic. The ratio $\text{Im}(N_\perp)/\text{Re}(N_\perp) \approx 0.15$ (see Fig. 7). The weak-damping condition is violated, and the ray trajectory is no longer physical. If Y is increased (or equivalently, if ω/Ω_e is decreased) such that the ray trajectory moves closer to the 1st harmonic resonance, this problem becomes more severe. Figure 8 demonstrates how the non-relativistic ray can acquire a group velocity faster than light for $Y > 0.82$ (equivalently, $\omega/\Omega_e < 1.22$). In contrast, with relativistic effects included, the 1st harmonic resonance is weakened. The relativistic ray can therefore penetrate further into the plasma without breaking the weak-damping approximation. As will be shown in Section 3, this effect can preclude ray-tracing simulations of non-relativistic EBWs as they approach the low-field-side harmonic in STEP.

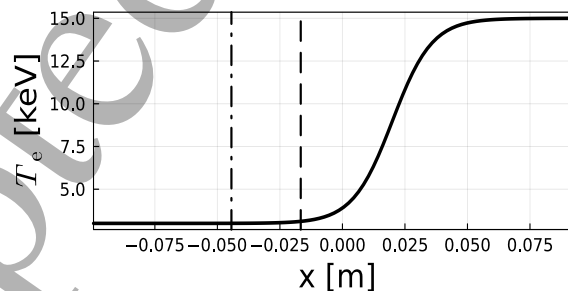


Figure 5: Modified slab geometry with tapered T_e profile. Solid vertical line denotes O-mode density cutoff. Dash-dotted vertical line denotes the UHR.

So far, the impact of relativistic effects on wave polarisation has not been commented on. Figure 9 plots the electric field components for the $T_e = 15\text{keV}$ case. There is a small impact on E_\parallel and negligible impact on E_- . A study of this effect by Nelson-Melby *et al.* [11] found this effect to be much larger. However, in that study, rays were evolved in a toroidal geometry and thus N_\parallel was not kept constant. This indicates that the *direct* impact of relativistic effects on wave polarisation is small. The *indirect* impact, via a

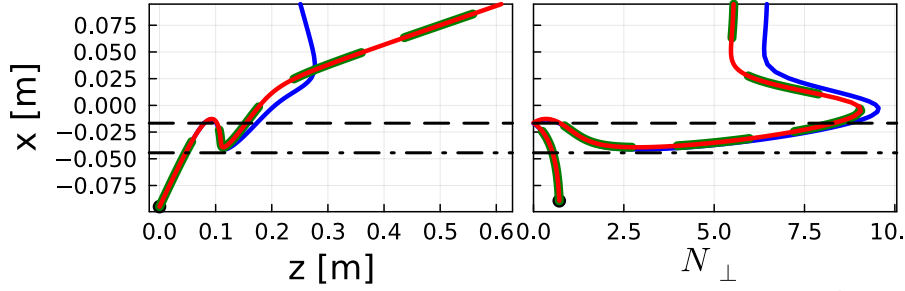


Figure 6: Ray trajectories in modified slab geometry (see Figs. 2 and 5). Blue: non-relativistic. Red: KK. Green dashed: Trubnikov 2nd Form. Dashed line denotes the O-Mode cutoff. Dash-dotted line denotes the UHR.

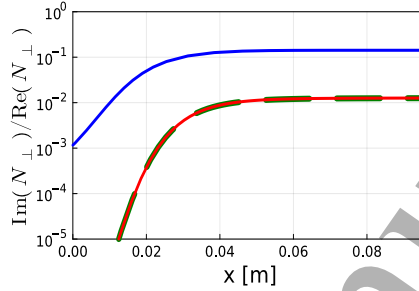


Figure 7: Imaginary perpendicular refractive index, normalised to real component, along rays in a modified slab geometry (see Figs. 2 and 5). Blue: non-relativistic. Red: KK. Green dashed: Trubnikov 2nd Form.

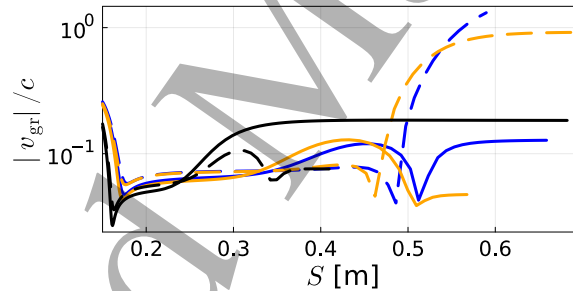


Figure 8: Group velocity versus distance along the ray trajectory (S) for $\omega/\Omega_e = 1.21$ (blue), 1.22 (orange), and 1.3 (black). Solid and dashed lines denote relativistic and non-relativistic rays, respectively. Using the modified slab geometry (see Figs. 2 and 5).

modified phase-space trajectory, can be much larger.

It should also be noted that the choice of dispersion shifts the O-mode cutoff density away from $\omega = \omega_{pe}$. This effect grows with T_e . The new cutoff can be approximated by evaluating $\omega = \omega_{pe}$ with a relativistic mass correction $m_e \rightarrow \gamma m_e$, where γ is evaluated at $v_{te} = \sqrt{T_e/m_e}$. For the temperatures under consideration, these shifts are at sub-millimetre scales. For example, they are only perceptible in the slab ray trajectories plotted in this section if zoomed in at the cutoff. This should have negligible impact on O-X mode-conversion in STEP.

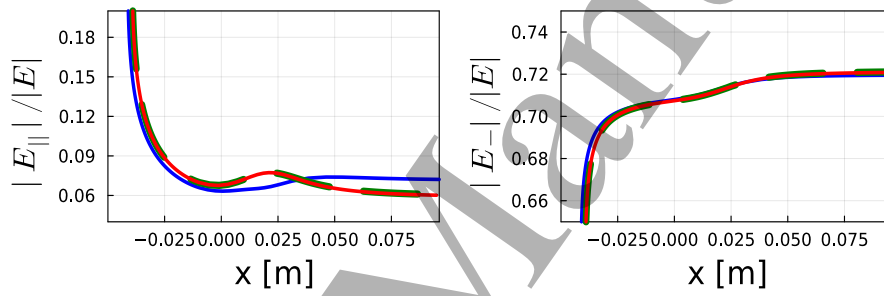


Figure 9: Wave polarisation along rays in a modified slab geometry (see Figs. 2 and 5). The component $E_{\parallel} = E_z$ and E_- is the right-hand polarisation. Blue: non-relativistic. Red: KK. Green dashed: Trubnikov 2nd Form.

4 EB CD modelling in STEP geometry

Electron Bernstein wave current drive performance - between the 1st and 2nd cyclotron harmonics - is scoped for a conceptual STEP operation point. (Note that this plasma is different from the one modelled in our earlier analysis [18].) It is similar to the EB CD+ECCD “conservative confinement” steady-state operating point (a.k.a. EB-CC) detailed in Tholerus *et al.* [4] With a bootstrap fraction of $\sim 81\%$, roughly 4 MA must be driven externally. (Please refer to Table 5 and Fig. 16 in [4] for the target current drive requirements.) Figures 10 and 11 summarise the parameters and geometry of this plasma. A Z_{eff} of 2.5 is assumed everywhere. For the assumed microwave frequencies, the 1st harmonic resonance occurs on the inboard side, but can be accessed at larger R due to Doppler broadening. Likewise, the Doppler broadened 2nd harmonic can be accessed as the EBW passes through the magnetic well near the outer mid-plane (visible in Fig. 10b). The 2nd harmonic is easier to access at higher microwave frequencies.

We have conducted a ray-tracing scan over launch parameters to find the optimal point(s) that maximise CD efficiency. In the case of optimal O-X-B mode conversion, the wave $|N_{\parallel}|$ at the O-mode cutoff ($\omega = \omega_{\text{pe}}$) is already constrained: it should approach $N_{\parallel, \text{opt}} = \sqrt{Y/(1+Y)}$ [1]. This constraint results in two free parameters for the microwave ray trajectory: frequency and poloidal launch height. We limit ourselves to considering microwave launch between 85 and 105 GHz. As seen in Fig. 10, frequencies above 105 GHz will move the O-mode cutoff well into the plasma, past the pedestal, where a high L_n will degrade the O-X mode-conversion efficiency. Likewise, frequencies below 90 GHz will move the upper-hybrid frequency (UHR) into the SOL, especially farther from the mid-plane. This should be avoided, given uncertainties in the SOL profile and the possibility of parasitic edge losses (i.e. collisional damping and parametric decay [25, 26]). For the purposes of exploring relativistic effects, we have extended the scan down to 85 GHz to capture an interesting class of rays that damp near-axis, further discussed in Section 4.1.

The poloidal launch height is scanned via prescribing Z_{OX} , which is the Z coordinate (in R, ϕ, Z cylindrical coordinates) where the O-X mode-conversion takes place at the O-mode cutoff. At this point, N_{\parallel} is set to $N_{\parallel, \text{opt}}$ and \mathbf{N}_{\perp} is simply zero. From this location the X-mode is evolved forward in time; it will initially travel into the plasma, then travel out towards the UHR, before mode-converting to the EBW and propagating into the core. In contrast, the O-mode is evolved backwards in time to determine the position and orientation of the external launcher. In this way, optimal O-X-B launch is forced in the simulation. From Fig. 10, it is evident that the upper hybrid resonance can be significantly outside the last closed flux surface (LCFS) for values of Z_{OX} far from the mid-plane. Thus, the scan is limited to values of Z_{OX} in the range -3.2 and +3.2m.

The 2D scan (f, Z_{OX}) determines all ray trajectories of interest for outboard O-X-B launch. An adjoint model [18] is used to provide a rough estimate for CD efficiency. It captures both Fisch-Boozer [27] and Ohkawa [28] current-drive mechanisms, the latter of which is expected to be dominant far off-axis. The adjoint model is expected to fail for experimentally-relevant power levels, at which point quasilinear effects will impact CD location and efficiency. The quasilinear power threshold in STEP is expected to be $\sim 1\text{MW}$ launched microwave power [18], far below what is required for fully non-inductive operation. Section 4.2 briefly discusses quasilinear effects in STEP.

Figure 12 plots relativistic ray trajectories at three separate frequencies. The rays terminate when they have damped 99.9% of their initial power. While most rays terminate far off-axis ($\rho > 0.7$), some rays above the mid-plane can propagate as deep as $\rho \approx 0.3$. It should be noted that at each OX mode-conversion point, there are two optimal wave-vector orientations. They correspond to $N_{\parallel} = \pm N_{\parallel, \text{opt}}$ where $N_{\parallel, \text{opt}} = \sqrt{Y/(1+Y)} > 0$.

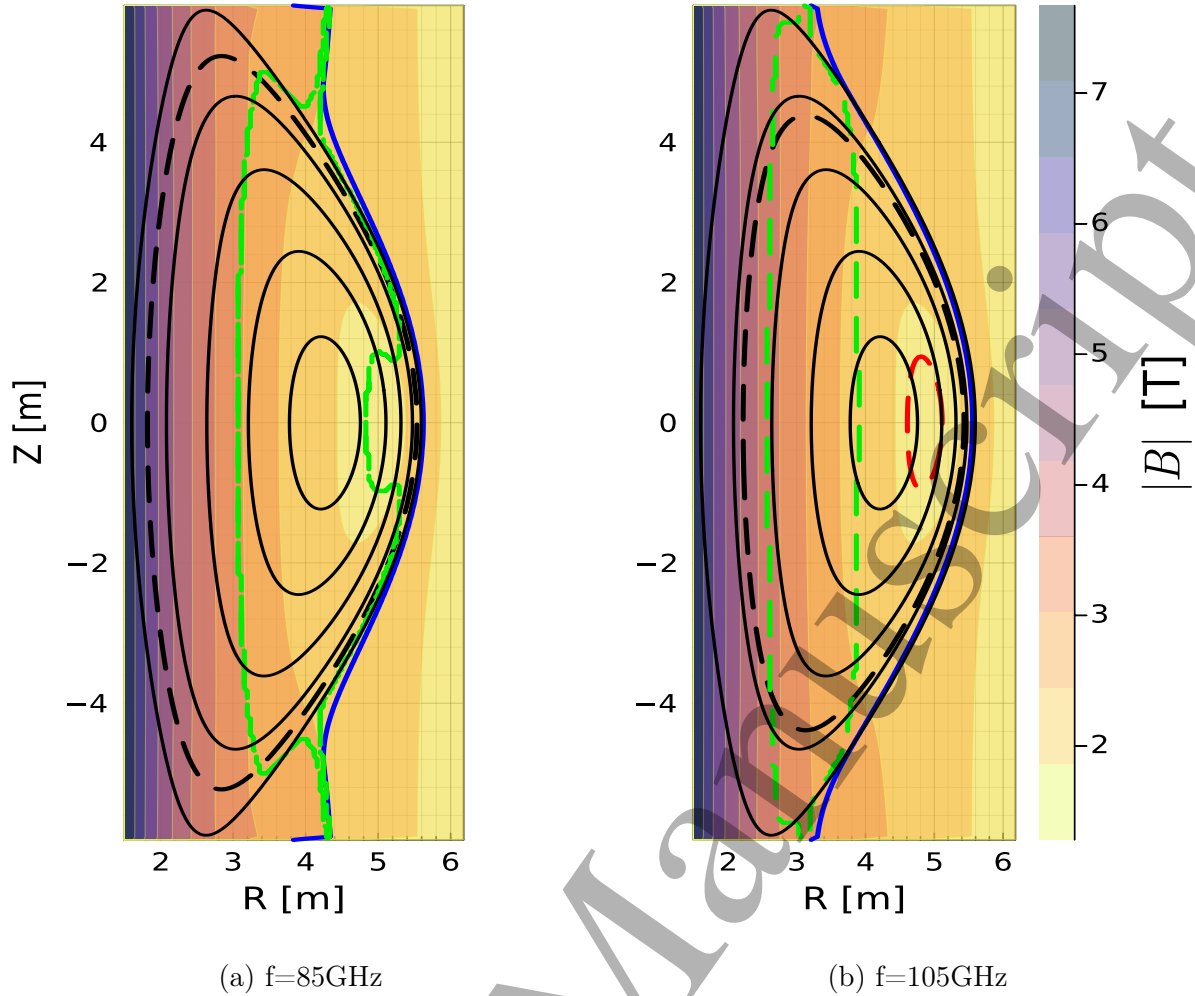


Figure 10: Poloidal cross-section of STEP plasma. Area in dashed green (red) contour denotes region of strong Doppler-broadened first (second) harmonic resonance, as determined by $\omega = n\Omega_e \pm 3v_{Te}k_{\parallel}$ for $N_{\parallel} = 0.5$. Resonance contours correspond to microwave frequencies of 85GHz (left) and 105GHz (right). Black dashed contour denotes O-mode cutoff. Solid blue line denotes UHR. Solid black contours denote flux surfaces in increments of 0.2ρ . Colorbar shows contours of total magnetic field. Toroidal magnetic field and plasma current are oriented counter-clockwise when viewed top-down.

The scans shown use $N_{\parallel} = +N_{\parallel,\text{opt}}$. The STEP equilibrium is top-down symmetric with respect to the mid-plane ($Z = 0$). As a result, a scan using $N_{\parallel} = -N_{\parallel,\text{opt}}$ results in a variant of Figure 12 where the rays are flipped along the mid-plane. They also travel in the opposite toroidal direction and therefore drive current in the reverse direction.

Figure 13 plots the radial location of peak power deposition and the total current driven - both as functions of f and Z_{OX} . Rays are shown to most commonly damp far off-axis. The exception is a group of rays launched above the mid-plane. This can be attributed to an initial downshift of $|N_{\parallel}|$ following O-X mode-conversion, which narrows the Doppler broadened 2nd harmonic and therefore weakens strong resonant damping at the edge. In some cases, the ray may propagate far enough to damp near axis at the 1st harmonic. In contrast, rays launched below the mid-plane undergo an $|N_{\parallel}|$ upshift, leading to swift resonant damping at the edge. This is explored in more detail in Section 4.1.

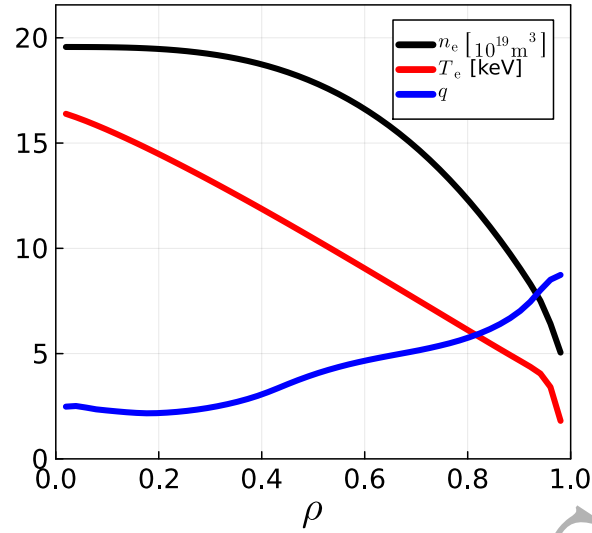


Figure 11: Radial equilibrium profiles in the plasma, where $\rho \propto \sqrt{\psi_{\text{tor}}}$.

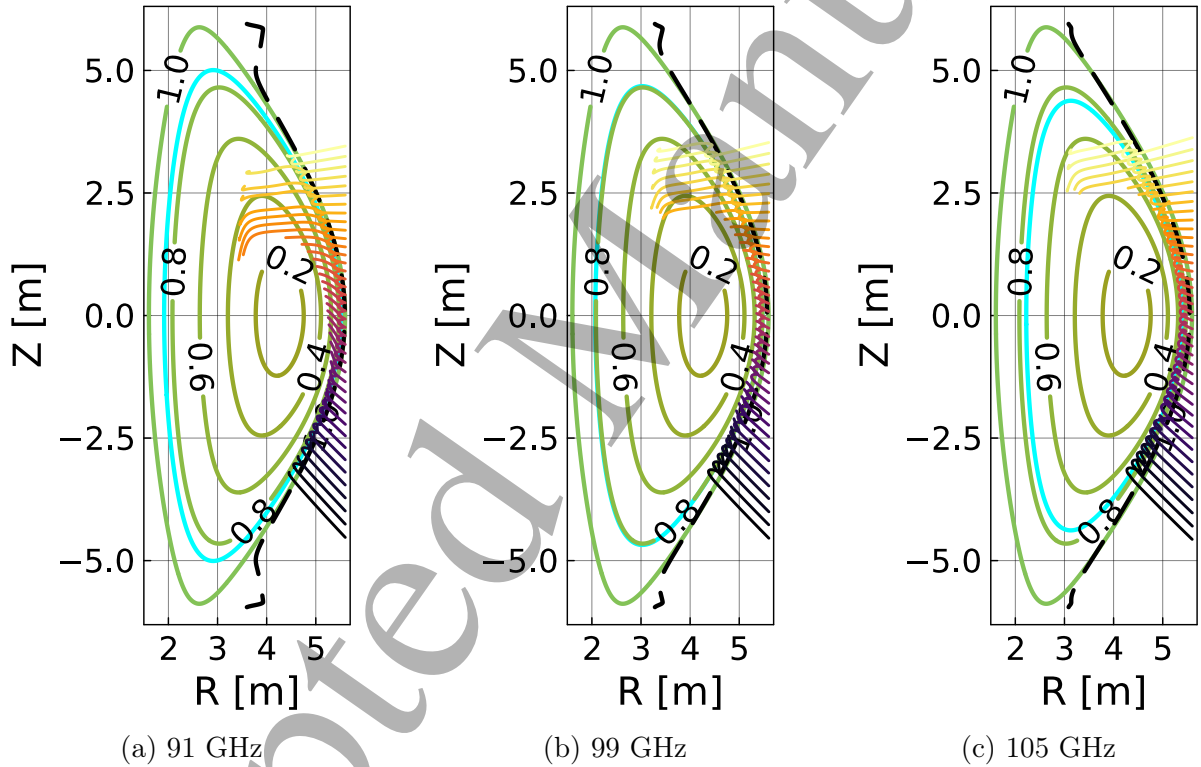


Figure 12: Poloidal projection of ray trajectories in real-space. Colours represent different Z_{OX} . Black dashed line denotes UHR. Cyan contour denotes the O-mode cutoff.

Current-drive is maximised for rays with $f \approx 98\text{GHz}$ and $Z_{OX} \approx -1\text{m}$. Figure 14 reveal that these below mid-plane launch parameters predominantly lead to strong damping on the 2nd harmonic, and therefore drive current predominantly through the Ohkawa mechanism. At lower frequencies, the damping mechanism smoothly transitions to far off-axis 1st harmonic damping, which can be either Ohkawa or Fisch-Boozer dominant. Concurrent 1st and 2nd harmonic damping is possible due to a large Doppler broadening of both resonances. It is found that off-axis 1st harmonic damping is not particularly

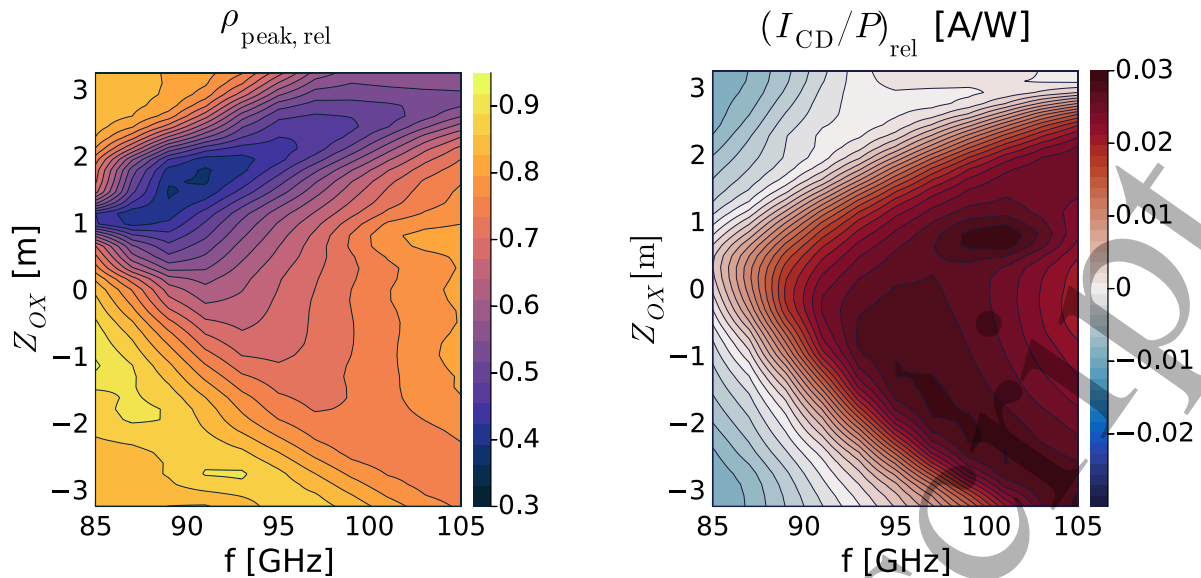


Figure 13: Left: Radial location of peak power deposition. Right: Total current driven assuming 1MW of launched microwave power. $I_{\text{CD}} > (<)$ 0 denotes co- (counter-) current drive.

attractive for this STEP operating point.

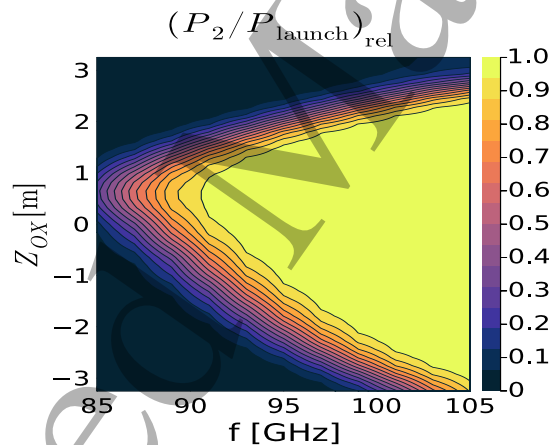


Figure 14: Fraction of launched power damped at the 2nd harmonic. Remaining power is damped at the 1st harmonic.

4.1 Importance of relativistic ray trajectories

It is worthwhile to inspect a few exemplar rays to better understand their phase-space evolution and other factors impacting CD location and efficiency. It would also be helpful to determine when relativistic propagation effects matter. Hence, the previous linear scan is repeated but with non-relativistic ray trajectories. In the non-relativistic simulations, resonant damping is still calculated relativistically. For details, see Appendix B. This “mixed” approach is taken for two reasons. (1) Relativistic effects are known to strongly impact *damping*, even in present-day devices. Thus, this mixed approach is the standard method in existing EBW ray-tracers. (2) In comparing against the mixed approach, the impact of relativistic *propagation* is isolated.

These studies reveal three notable classes of rays.

Near axis (NA) rays: The first class of rays are categorised as “Near Axis” damping, or NA, rays. See Figs. 15 and 16 for examples of such rays at 87GHz. These rays are launched above the mid-plane such that they initially undergo an $|N_{||}|$ downshift following O-X mode-conversion. Eventually, they pass through $N_{||} = 0$ at $\rho < 0.4$. Next, $|N_{\perp}|$ increases as the ray approaches the 1st harmonic. Sufficiently close to the 1st harmonic, the ray will strongly damp the remainder of its power.

Figures 15 and 16 reveal significant differences between the non-relativistic and relativistic ray trajectories, in both real and phase-space. The disagreements begin near the UHR, as expected from slab modelling, and continue to grow as the EBW propagates further into core.

Of particular interest is the power deposition profile, as shown in Fig. 17. Both relativistic and non-relativistic simulations capture the partial ray damping far off-axis at the 2nd harmonic. Only the relativistic simulation captures the strong 1st harmonic damping near $\rho = 0.3$; the non-relativistic rays terminate prematurely due to numeric errors.

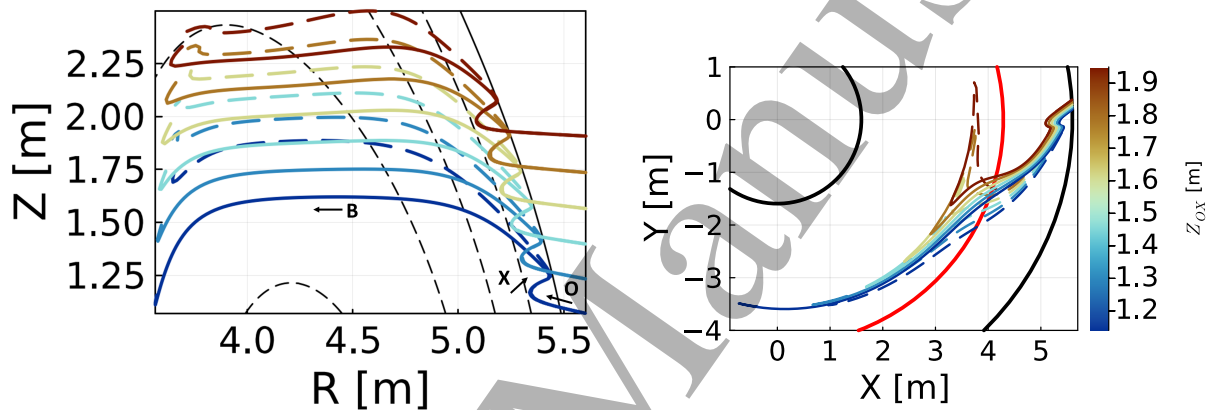


Figure 15: Near axis (NA) rays at 87GHz. Poloidal (a) and top-down (b) projection of ray trajectories. Solid: relativistic. Dashed: non-relativistic. In (a), black dashed curves show flux surfaces and the black solid curve shows the LCFS. The propagation directions in the poloidal plane of O, X and B waves are indicated by arrows. In (b), the solid red curve indicates the magnetic axis and the solid black curves indicates where the LCFS intercepts the mid-plane.

This numeric issue is related to that discussed in Section 3. The relativistic rays make a low-field-side approach to the 1st harmonic and promptly damp all remaining power according to the relativistic damping model. The non-relativistic rays also approach the 1st harmonic but do not fully damp, at least according to the *mixed* damping model. They instead terminate prematurely with $\sim 75\%$ of power un-damped. This is because the non-relativistic rays violate the weak-damping approximation well before the mixed-relativistic damping becomes significant. As a result, the rays begin propagating faster than light, causing the ray-tracer to terminate with an error.

The numeric issue discussed above prevents the non-relativistic ray-tracing of NA rays. These are also particularly interesting rays because they propagate so far into the plasma. Naturally, one hopes that relativistic ray-tracing will reveal high CD efficiencies close to the magnetic axis. This is unfortunately not the case, as small CD efficiencies of $\eta \approx 0.001A/W$ are realised near-axis. In normalised units [29], this corresponds to $\zeta_{CD} \equiv 32n_{20}R\eta_{A/W}T_{keV} \approx 0.08$. These rays are strongly damped near the “pinch-point,”

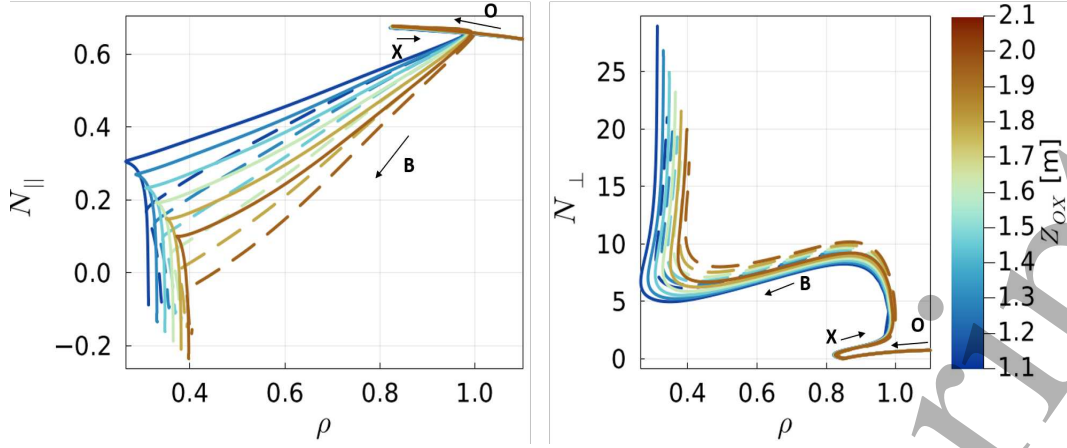


Figure 16: NA rays: Ray trajectories in phase-space. Solid: relativistic. Dashed: non-relativistic

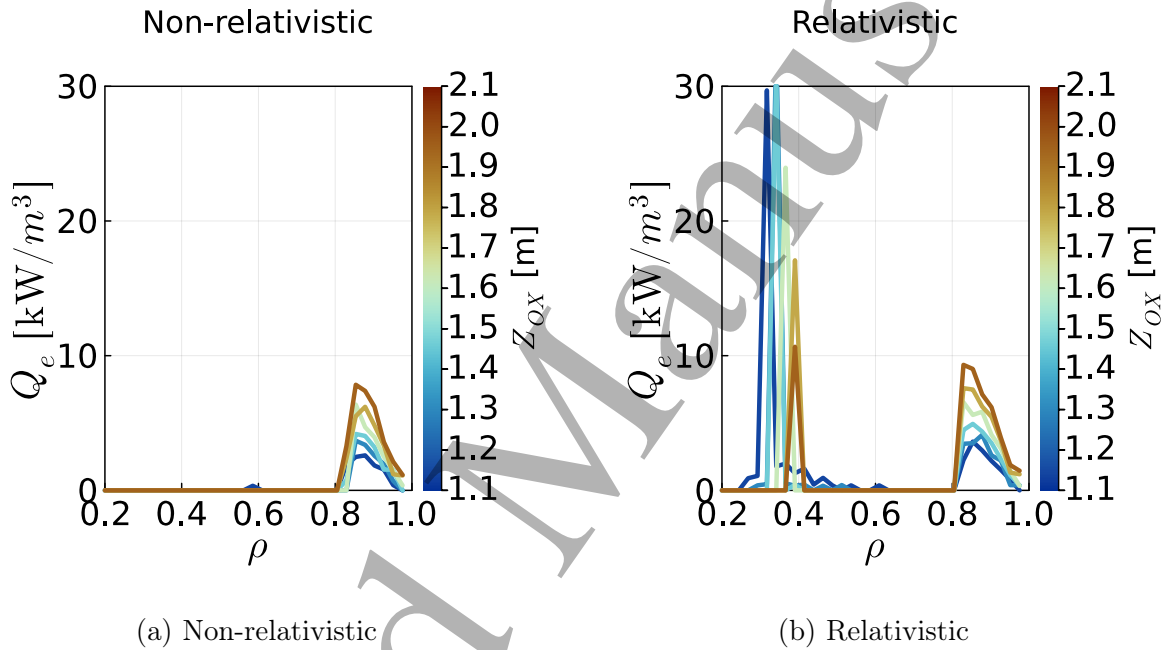


Figure 17: NA rays: Power deposition profiles for 1MW ray. $f=87\text{GHz}$. Near-axis power deposition (at $\rho \approx 0.3$) is expected in both the non-relativistic and relativistic simulations. However, the non-relativistic rays terminate prematurely due to numeric errors.

the point at which the low-field-side resonance first becomes accessible (and then only for electrons with zero pitch angle). This point corresponds to:

$$n_-^2 Y^2 + N_{\parallel}^2 = 1 \quad (11)$$

where n_- is the low-field-side harmonic (i.e. $n_- = 1$). Substituting this into the wave-particle resonance condition reveals that the pinch-point corresponds to resonant particles with $v/v_{te} = c|N_{\parallel}|nY/(v_{te}(1 - N_{\parallel}^2))$, where $v_{te} = \sqrt{T_e/m_e}$. Thus, resonant particle speed at the pinch-point is linearly proportional to $|N_{\parallel}|$. Given $|N_{\parallel}| \approx 0.2$ at the pinch-point (see Fig. 16), this corresponds to electron velocities of $v/v_{te} \approx 1.5$. These electrons are practically thermal, and therefore highly collisional and not attractive for driving current. One could therefore consider this an electron heating scheme.

Off-Axis (OA) rays: The 2nd class of rays are labelled Off-Axis (OA) rays because

they deposit power in the region of $0.4 < \rho < 0.7$ at the 2nd harmonic. Since these rays make a high-field-side approach to the cyclotron resonance, they are not susceptible to the same numeric issues plaguing NA rays in non-relativistic simulations. Nevertheless, there is a significant difference in ray trajectories between the non-relativistic and relativistic cases, as seen for launch above the mid-plane at 91GHz (see Fig. 18). Again, the discrepancy starts to become noticeable at the X-B mode-conversion near the UHR.

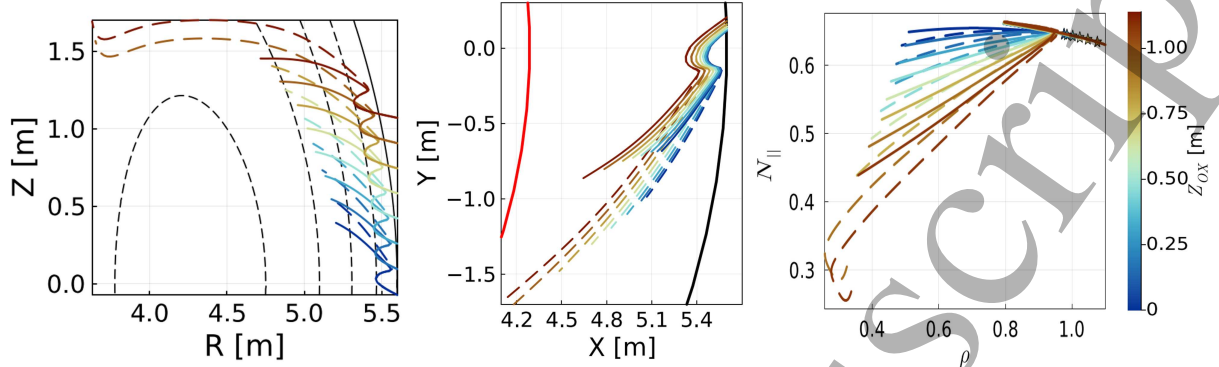


Figure 18: Off-axis (OA) rays at 91GHz. Poloidal (left) and top-down (middle) projection of ray-trajectories. Right plot shows trajectories in phase-space. Solid: relativistic. Dashed: non-relativistic.

At 91GHz, both the relativistic and non-relativistic simulations predict a decrease in CD efficiency as Z_{OX} increases (see Fig. 19). There is, however, a quantitative mismatch in driven current. This mismatch grows as Z_{OX} increases and the power-deposition peak moves inwards. At $Z_{OX} \approx +1.2\text{m}$, the relativistic case predicts $\sim 200\%$ higher CD efficiency (0.014 A/W versus 0.0045 A/W).

Far Off-axis (FOA) rays: The 3rd class of rays are labeled Far Off-Axis (FOA) rays because they damp near the plasma edge ($\rho > 0.7$). Figure 20 plots example ray trajectories for below mid-plane launch at $f=101\text{GHz}$. Once again, discrepancies between the relativistic and non-relativistic cases start to become noticeable at the X-B mode conversion. Concurrently, these rays undergo a large $|N_{||}|$ -upshift. Hence, they very quickly damp in the edge. Given that these trajectories are relatively short, there is little *cumulative* disagreement between the relativistic and non-relativistic trajectories. In turn, there is little disagreement in the current drive profiles (see Fig. 21). In other words,

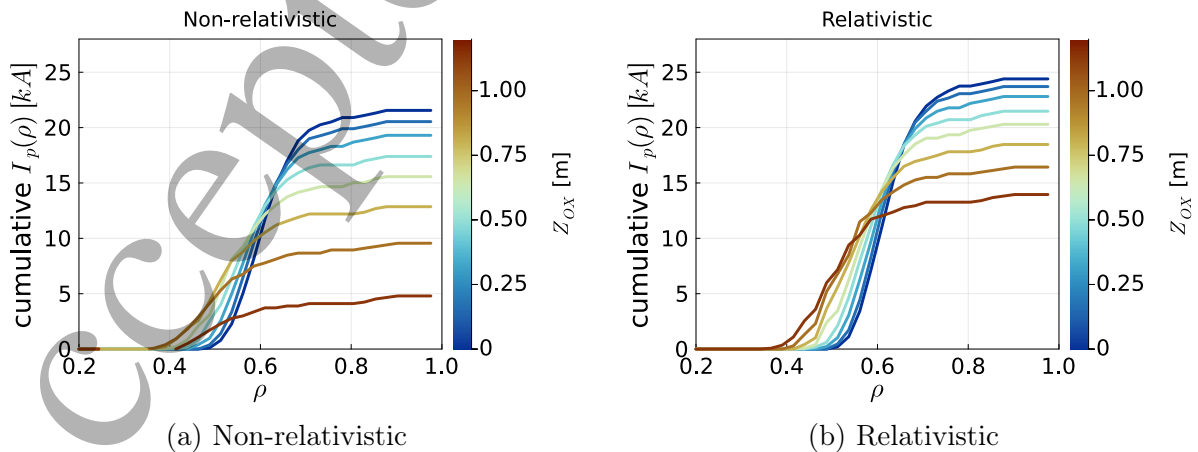


Figure 19: OA rays: Cumulative driven current profile for 1MW ray. Linear CD model used. $f=91\text{GHz}$.

toroidal effects and Doppler broadening seem to overshadow the impact of relativistic propagation. Furthermore, these launch parameters predict a robust, high CD efficiency of $\sim 0.03A/W$ localised to $\rho \approx 0.8$.

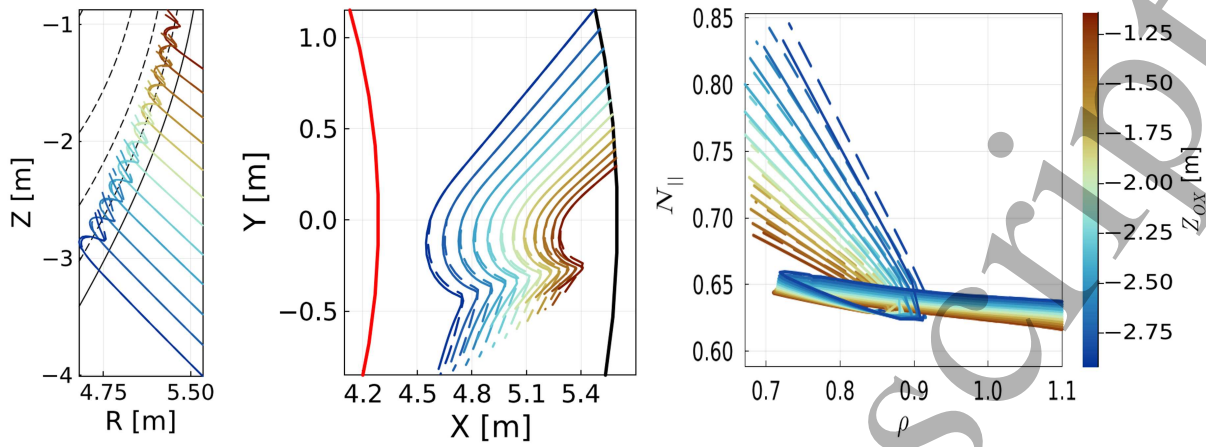


Figure 20: Far off-axis (FOA) rays at 101GHz. Poloidal (left) and top-down (middle) projection of ray-trajectories. Right plot shows trajectories in phase-space. Solid: relativistic. Dashed: non-relativistic.

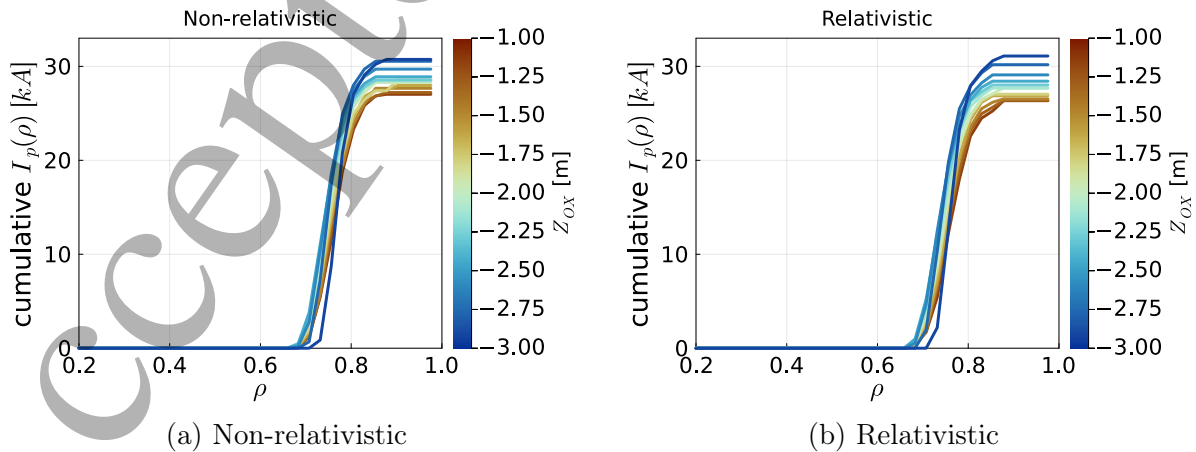


Figure 21: FOA rays: Cumulative driven current profile for 1MW ray. Linear CD model used. $f=101\text{GHz}$.

4.2 Quasilinear effects at high EBW power

The linear current drive model predicts maximum efficiency at $f \approx 98\text{GHz}$ and $Z_{OX} \approx -1\text{m}$. This corresponds to the FOA ray class, which suggests non-relativistic simulations are adequate. However, we have so far neglected quasilinear effects.

Quasilinearity here refers to how CD efficiency is a function of power at sufficiently high power. This is caused by the EBW modifying the electron distribution away from a Maxwellian. Verification of the EBW linear current drive model against CQL3D [19] reveals that quasilinear effects become important when $\langle E \rangle / \sqrt{n_{19} \ln \Lambda / 16} \gtrsim 50\text{V/cm}$, where $\langle E \rangle$ is the flux-surface averaged RF electric field amplitude, $n_{19} \equiv n_e / 10^{19}\text{m}^{-3}$, and $\ln \Lambda$ is the Coulomb logarithm [18]. This roughly translates to $\gtrsim 1\text{MW}$ of launched EBW power in STEP. On the other hand, $\gtrsim 100\text{MW}$ of EBW power is required for fully non-inductive steady state operation. It is therefore prudent to check how the conclusions above are impacted by quasilinearity.

A ray-tracing scan in (f, Z_{OX}) is conducted around the linear optimal point. Then the ray trajectories are coupled to CQL3D for another scan in launched ray power. The power-scan is done for 1kW , 1MW , 10MW , and 100MW . Quasilinear effects are only noticeable at $>1\text{MW}$. The result of this scan is presented in Figs. 22 and 23.

Figure 22 plots global CD efficiency (η) as a function of f , Z_{OX} , and launched EBW power. At lower power ($\leq 1\text{MW}$), there is good agreement with the linear adjoint model. With increasing power ($> 1\text{MW}$), the optimal launch point is shifted to lower frequencies and larger Z_{OX} . Assuming a 100MW beam, the new optimal launch point is moved to 91GHz and $Z_{OX} \approx -0.25\text{m}$. Furthermore, at 100MW , the *linear* optimal launch point sees a $\sim 27\%$ decrease in η .

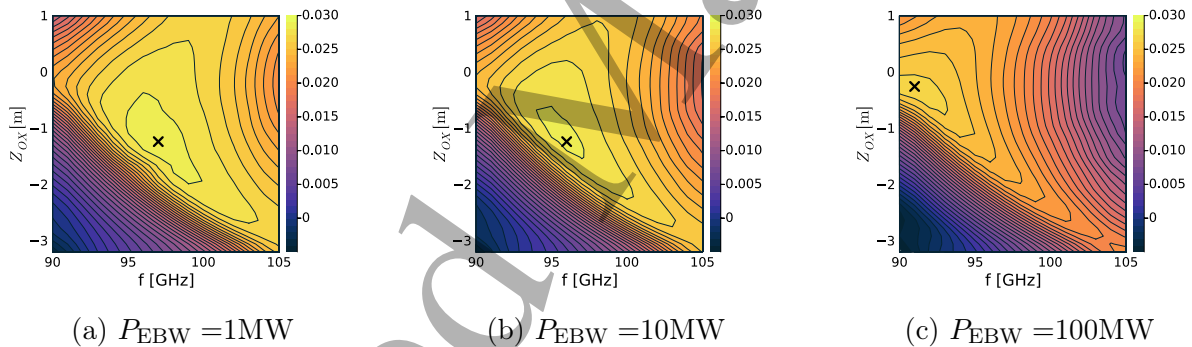


Figure 22: Global current drive efficiency $\eta = I_{CD}/P_{EBW}$ [A/W] as a function of frequency (f), launch height (Z_{OX}), and launched microwave power (P_{EBW}). Black cross indicates the optimal launch point at which η is maximised.

Figure 23 plots the radial location for maximum $|j_{\text{tor}}|$ deposition. The general trend is for a radial shift inward as power increases. This is as expected, because the wave-particle interaction is a diffusive term that decreases $|\nabla_{\mathbf{v}} f_e|$ at the resonance. In turn, wave damping will saturate at high powers, allowing for deeper penetration of the beam into the plasma. This effect is most noticeable for above mid-plane launch at $90\text{-}95\text{GHz}$, where the peak ρ shifts by -0.05 between the 1MW and 100MW case. Notably, the new optimal launch point corresponds to a peak deposition at $\rho \approx 0.6$. This is safely in the OA class of rays, indicating that relativistic effects are important.

It should be emphasised that quasilinearity only impacts ray damping and the current response; it does not impact the ray trajectory. However, in taking account for quasilinear effects, the optimal launch point (that which maximised η) is shifted from the FOA ray class to the OA ray class.

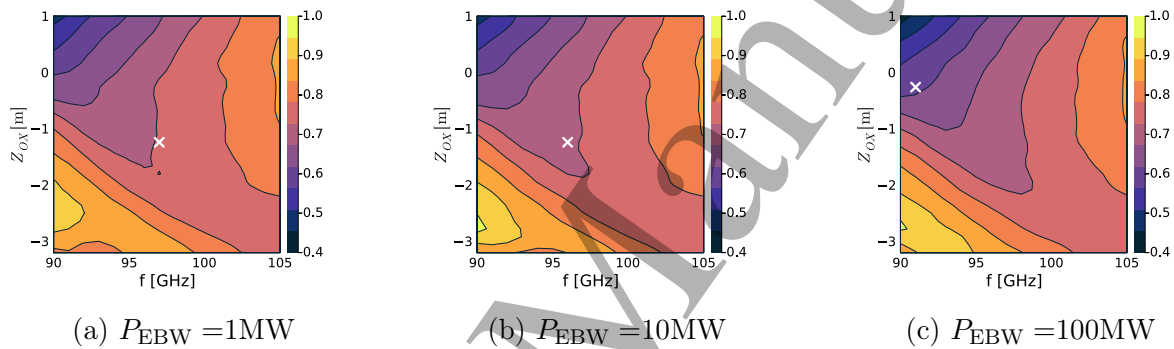


Figure 23: Radial location of peak current deposition as a function of frequency (f), launch height (Z_{ox}), and launched microwave power (P_{EBW}). White cross indicates the optimal launch point at which η is maximised.

5 Summary

Efficient evaluation of the fully-relativistic hot dispersion, via the KK relations, enables fast EBW ray-tracing simulations in reactor-relevant plasmas. Such a ray-tracer is being applied to the optimisation of the EBCD launcher in STEP.

Ray-traces of O-X-B mode-coupling in slab geometry verify that the KK dispersion exactly matches Trubnikov's 2nd Form, as it should. Slab runs indicate that relativistic modification to the ray trajectory becomes noticeable at the X-B mode-conversion and beyond. This effect grows with temperature. At $T_e \gtrsim 4\text{keV}$, one expects significant modification to the Bernstein wave. This is comparable to the pedestal temperature in STEP, and so further motivates the modelling of relativistic wave propagation in EBCD calculations.

Fully relativistic simulations of EBW ray propagation, damping, and current-drive have been conducted for a conceptual STEP steady-state operating point. To find all possible beam trajectories of interest, a 2D scan in frequency and poloidal launch height has been conducted. The parameter scan was restricted to outboard launch, and frequencies between 90 to 105 GHz to ensure efficient O-X-B coupling.

The relativistic EBCD simulations are compared against simulations in which ray-propagation is modelled in the non-relativistic limit. In both cases, damping is modelled relativistically (see Appendix B). Three particularly interesting classes of rays are identified. (1) Near-axis, or NA rays, propagate deep into the core and fully damp following a low-field-side approach of the 1st cyclotron harmonic. Relativistic effects weaken the low-field-side cyclotron resonance. In turn, non-relativistic ray trajectories become unphysical prior to fully damping because the weak-damping approximation breaks down. Thus, these rays reveal a parameter regime in which relativistic simulations are essential. NA rays are only possible for above mid-plane launch because this corresponds to an initial $|N_{\parallel}|$ down-shift. In turn, these rays avoid fully damping at the Doppler-broadened 2nd harmonic at larger ρ . Unfortunately, this $|N_{\parallel}|$ downshift also results in poor CD efficiency at the 1st harmonic. (2) Off-axis, or OA rays, propagate to mid-radius before fully damping at the 2nd harmonic through a high-field-side approach. This coincides with a weak evolution in N_{\parallel} . The high-field-side cyclotron resonance is strengthened through relativistic effects. Thus, issues with the weak-damping approximation in the non-relativistic limit are avoided. Nevertheless, significant disagreement in the ray trajectories and CD profiles persist. Thus, relativistic simulations are necessary for accurate predictions. (3) Far-off-axis, or FOA rays, refer to those with short trajectories that strongly damp at $\rho > 0.7$ following a strong $|N_{\parallel}|$ upshift. While the relativistic and non-relativistic trajectories start to diverge following the X-B conversion, the rays are too short for this to matter. A subset of these rays also exhibit high current drive efficiency.

Linear parametric scans suggest that global CD efficiency is maximised near 98GHz and $Z_{OX} = -1\text{m}$, resulting in $\eta \approx 0.03\text{A/W}$, or $\zeta_{CD} \approx 0.6$ in normalised units. Current-drive would be localised to $\rho \approx 0.75$. This corresponds to the FOA class of rays, indicating relativistic propagation is not important at the optimal launch point. However, preliminary quasilinear modelling at reactor-relevant microwave powers indicate the optimal launch point will be shifted to lower frequencies and higher Z_{OX} . In turn, the current peak is pushed inwards to $\rho \approx 0.6$. This corresponds to the OA class of rays, for which relativistic effects can significantly modify CD performance. We also note that, at this particular operating point with 100MW of EBW power, the new optimal launch point also results in $\eta \approx 0.03\text{A/W}$, but a slightly lower $\zeta_{CD} \approx 0.55$. This would enable the non-inductive drive of 4MA with around 130MW of injected power. Quasilinear predictions will be further explored in a future paper.

1
2 At low powers, the optimal region in (f, Z_{OX}) -space is fairly broad (see Fig.23a), which
3 indicates it is insensitive to small changes in launcher design and plasma parameters. At
4 high powers (see Fig.23c), the optimal region shrinks, indicating that CD performance is
5 relatively less robust. Strictly speaking, the O-X coupling window must also be taken into
6 account. That is a separate - albeit important - consideration and is outside the scope of
7 this work.
8

9 Three large caveats must be explicitly stated about the conclusions drawn above.
10 First, these simulations assume perfect O-X-B mode-conversion by virtue of enforcing
11 the optimal $N_{||}$ at the O-mode cutoff. In reality, full-wave effects, including finite beam
12 width, will result in a mode-conversion efficiency that is less than unity. Thus, full-wave
13 calculations of the mode-conversion window are required to understand how practical each
14 launch point really is. Second, the plasma parameters have been kept fixed. It would be
15 prudent to determine how CD performance changes as a result of small variations to the
16 plasma equilibrium. The work herein has developed a method for solving fully-relativistic
17 ray trajectories in minutes, as opposed to hours. This speed-up will further facilitate
18 these parametric scans. Lastly, it is worthwhile to consider that the quasilinear treatment
19 of the wave-particle resonance may be invalid, especially for high-power, highly localized
20 microwave beams [30]. This consideration is outside the scope of this paper, but important
21 to address in future work.
22

23 Lastly, one must comment on the necessity of relativistic ray-tracing in present-day
24 devices. The model described in this paper was applied to a typical MAST-U discharge
25 ($T_{e0} \approx 2\text{keV}$) for near-axis current-drive. The error in non-relativistic rays was negligible.
26 High temperature ($T_e \gtrsim 4\text{keV}$) is necessary, but not sufficient, for a large relativistic
27 impact. As demonstrated in this paper, ray length is also a factor.
28
29
30
31

32 Acknowledgements

33 This work has been funded by STEP, a UKAEA programme to design and build a proto-
34 type fusion energy plant and a path to commercial fusion.
35
36
37
38

39 Declaration of interest

40 The authors report no conflict of interest.
41
42
43
44
45
46
47
48
49
50
51
52
53
54
55
56
57
58
59
60

A Details of ray propagation

Propagation is modelled via the well-known geometrical optics equations [21]:

$$\frac{d\mathbf{r}}{dt} = -\frac{\partial D^H(\mathbf{r}, \mathbf{k}, \omega)/\partial \mathbf{k}}{\partial D^H(\mathbf{r}, \mathbf{k}, \omega)/\partial \omega} \quad (\text{A.1a})$$

$$\frac{d\mathbf{k}}{dt} = \frac{\partial D^H(\mathbf{r}, \mathbf{k}, \omega)/\partial \mathbf{r}}{\partial D^H(\mathbf{r}, \mathbf{k}, \omega)/\partial \omega} \quad (\text{A.1b})$$

where D^H is the Hermitian component of the dispersion relation (a.k.a. the ray Hamiltonian). Heuristically, ray-tracing is valid as long as the wavelength is much shorter than the characteristic length scale of the plasma. The weak-damping condition ($|\text{Im}(k_\perp)| \ll \text{Re}(k_\perp)$) must also be satisfied. The above equations are solved using a 4th order Runge-Kutta scheme.

In the slab geometry of Section 3, the ray-tracing equations are solved in Cartesian coordinates (x, y, z) and (k_x, k_y, k_z) . Since the plasma is homogeneous in the y and z direction, it follows that k_y and k_z are constant.

In the toroidal geometry of Section 4, the ray-tracing equations are solved in cylindrical coordinates (R, ϕ, Z) and (k_R, k_ϕ, k_Z) . Since the plasma is assumed axisymmetric (homogeneous along ϕ), it follows that Rk_ϕ is constant.

B Details of ray damping

The perpendicular damping coefficient along a ray is proportional to $\text{Im}(k_\perp)$, which is calculated via the weak-damping approximation

$$\text{Im}(k_\perp) \approx -\frac{D^{AH}}{\partial D^H/\partial k_\perp} \Big|_{k_\perp=\text{Re}(k_\perp)} \quad (\text{A.2})$$

where D^H is the Hermitian part of the Hamiltonian, and D^{AH} is the anti-Hermitian part. One advantage of the above approximation is that the Hermitian and anti-Hermitian terms are un-coupled. The denominator in the right-hand side of eq. A.2 is sensitive to how close $\text{Re}(k_\perp)$ is to the root of D^H . Since the ray-tracing equations provide $\text{Re}(k_\perp)$, the choice of D^H in eq. A.2 should match eqs. A.1. The choice of D^{AH} is usually less critical. In this paper, relativistic simulations refer to the use of the relativistic dispersion in both the numerator and denominator. This is self-consistent. For non-relativistic ray trajectories, one can either use the non-relativistic dispersion everywhere, or take a ‘‘mixed’’ approach. In the mixed approach, one uses the non-relativistic D^H and the relativistic D^{AH} . This allows one to account for relativistic damping along non-relativistic trajectories. This is computationally efficient and therefore a common technique in other codes, like GENRAY [31]. However, this approach has serious shortcomings as the ray approaches the low-field side harmonic resonance in hot plasmas, as discussed in Sections 3 and 4.

References

- [1] H. P. Laqua, “Electron Bernstein wave heating and diagnostic,” *Plasma Physics and Controlled Fusion*, vol. 49, pp. R1–R42, Apr. 2007.
- [2] T. Wilson, S. Freethy, M. Henderson, A. Köhn-Seemann, I. Konoplev, S. Saarelma, D. Speirs, R. Vann, and the STEP team, “Electron Bernstein Wave (EBW) current drive profiles and efficiency for STEP,” *EPJ Web of Conferences*, vol. 277, p. 01011, 2023.
- [3] S. Freethy, L. Figini, M. Henderson, H. El-Haroun, B. Eliason, S. Gibson, K. Kirov, A. Köhn-Seemann, I. Konoplev, S. Saarelma, R. Sharma, D. Speirs, R. Vann, H. Webster, T. Wilson, and the STEP team, “Microwave current drive for STEP and MAST Upgrade,” *EPJ Web of Conferences*, vol. 277, p. 04001, 2023.
- [4] E. Tholerus, F. Casson, S. Marsden, T. Wilson, D. Brunetti, P. Fox, S. Freethy, T. Hender, S. Henderson, A. Hudoba, K. Kirov, F. Koechl, H. Meyer, S. Muldrew, C. Olde, B. Patel, C. Roach, S. Saarelma, G. Xia, and the STEP team, “Flat-top plasma operational space of the STEP power plant,” *Nuclear Fusion*, vol. 64, p. 106030, Oct. 2024.
- [5] G. Taylor, P. C. Efthimion, C. E. Kessel, R. W. Harvey, A. P. Smirnov, N. M. Ershov, M. D. Carter, and C. B. Forest, “Efficient generation of noninductive, off-axis, Ohkawa current, driven by electron Bernstein waves in high β , spherical torus plasmas,” *Physics of Plasmas*, vol. 11, pp. 4733–4739, Oct. 2004.
- [6] J. Urban, J. Decker, Y. Peysson, J. Preinhaelter, V. Shevchenko, G. Taylor, L. Vahala, and G. Vahala, “A survey of electron Bernstein wave heating and current drive potential for spherical tokamaks,” *Nuclear Fusion*, vol. 51, p. 083050, Aug. 2011.
- [7] A. K. Ram, J. Decker, and Y. Peysson, “On electron Bernstein waves in spherical tori,” *Journal of Plasma Physics*, vol. 71, p. 675, Sept. 2005.
- [8] B. Trubnikov, *Plasma Physics and the Problem of Controlled Thermonuclear Reactions Vol III*. Permagon, 1959.
- [9] I. Weiss, “Electromagnetic wave propagation in relativistic magnetized plasmas,” *Journal of Computational Physics*, vol. 61, pp. 403–416, Dec. 1985.
- [10] J. Decker and A. K. Ram, “Relativistic description of electron Bernstein waves,” *Physics of Plasmas*, vol. 13, p. 112503, Nov. 2006.
- [11] E. Nelson-Melby, R. W. Harvey, A. P. Smirnov, and A. K. Ram, “Relativistic ray-tracing of electron Bernstein waves in a spherical tokamak reactor,” *Plasma Physics and Controlled Fusion*, vol. 49, pp. 1913–1929, Nov. 2007.
- [12] A. C. Airoidi and A. Orefice, “Relativistic dielectric tensor of a Maxwellian plasma for electron cyclotron waves at arbitrary propagation angles,” *Journal of Plasma Physics*, vol. 27, pp. 515–524, June 1982.
- [13] I. P. Shkarofsky, “New representations of dielectric tensor elements in magnetized plasma,” *Journal of Plasma Physics*, vol. 35, pp. 319–331, Apr. 1986.
- [14] D. G. Swanson, “Exact and moderately relativistic plasma dispersion functions,” *Plasma Physics and Controlled Fusion*, vol. 44, pp. 1329–1347, July 2002.

- 1
2 [15] A. N. Saveliev, "Approximate relativistic dispersion relation for electron Bernstein
3 waves in a Maxwellian plasma," *Plasma Physics and Controlled Fusion*, vol. 47,
4 pp. 2003–2017, Nov. 2005.
5
6 [16] F. Volpe, "Weakly relativistic dielectric tensor for arbitrary wavenumbers," *Physics
7 of Plasmas*, vol. 14, p. 122105, Dec. 2007.
8
9 [17] S. Pavlov and F. Castejon, "The fully relativistic dielectric tensor for arbitrary wave
10 vectors," *Nuclear Fusion*, vol. 58, p. 126030, Dec. 2018.
11
12 [18] B. Biswas, D. Speirs, S. Freethy, and R. Vann, "Application of linear electron Bern-
13 stein current drive models in reactor-relevant spherical tokamaks," *Nuclear Fusion*,
14 vol. 63, p. 126011, Dec. 2023.
15
16 [19] R. W. Harvey and M. G. McCoy, "The CQL3D Fokker-Planck Code (reconstituted in
17 editable form from General Atomics Report GA-A20978, 1992)," tech. rep., 2005.
18
19 [20] D. G. Swanson, *Plasma Waves*. Series in Plasma Physics, Bristol ; Philadelphia:
20 Institute of Physics Pub, 2nd ed ed., 2003.
21
22 [21] T. H. Stix, *Waves in Plasmas*. Springer Science & Business Media, 1992.
23
24 [22] H. Kramers, "La diffusion de la lumiere par les atomes.," *Atti Cong. Intern. Fisica
25 (Transactions of Volta Centenary Congress)*, vol. 2, 1927.
26
27 [23] R. Kronig, "On the theory of dispersion of x-rays," *Josa*, vol. 12, no. 6, 1926.
28
29 [24] M. Brambilla, *Kinetic Theory of Plasma Waves: Homogeneous Plasmas*. Oxford
30 University Press, 1998.
31
32 [25] S. J. Diem, G. Taylor, J. B. Caughman, P. C. Efthimion, H. Kugel, B. P. LeBlanc,
33 C. K. Phillips, J. Preinhaelter, S. A. Sabbagh, and J. Urban, "Collisional Damping
34 of Electron Bernstein Waves and its Mitigation by Evaporated Lithium Conditioning
35 in Spherical-Tokamak Plasmas," *Physical Review Letters*, vol. 103, p. 015002, June
36 2009.
37
38 [26] H. P. Laqua, V. Erckmann, H. J. Hartfuß, and H. Laqua, "Resonant and Nonresonant
39 Electron Cyclotron Heating at Densities above the Plasma Cutoff by O-X-B Mode
40 Conversion at the W7-As Stellarator," *Physical Review Letters*, vol. 78, pp. 3467–
41 3470, May 1997.
42
43 [27] N. J. Fisch and A. H. Boozer, "Creating an Asymmetric Plasma Resistivity with
44 Waves," *Physical Review Letters*, vol. 45, pp. 720–722, Sept. 1980.
45
46 [28] T. Ohkawa, "Steady-state operation of tokamaks by rf heating," *General Atomics
47 Report GA-A13847*, 1976.
48
49 [29] T. C. Luce, Y. R. Lin-Liu, R. W. Harvey, G. Giruzzi, P. A. Politzer, B. W. Rice, J. M.
50 Lohr, C. C. Petty, and R. Prater, "Generation of Localized Noninductive Current by
51 Electron Cyclotron Waves on the DIII-D Tokamak," *Physical Review Letters*, vol. 83,
52 pp. 4550–4553, Nov. 1999.
53
54 [30] R. Kamendje, S. V. Kasilov, W. Kernbichler, and M. F. Heyn, "Kinetic modeling of
55 nonlinear electron cyclotron resonance heating," *Physics of Plasmas*, vol. 10, pp. 75–
56 97, Jan. 2003.
57
58
59
60

- 1
2 [31] A. Smirnov and R. Harvey, “The GENRAY Ray Tracing Code,” tech. rep., CompX,
3 2001.
4
5
6
7
8
9
10
11
12
13
14
15
16
17
18
19
20
21
22
23
24
25
26
27
28
29
30
31
32
33
34
35
36
37
38
39
40
41
42
43
44
45
46
47
48
49
50
51
52
53
54
55
56
57
58
59
60

Accepted Manuscript